Electrochimica Acta 411 (2022) 139832

Contents lists available at ScienceDirect

Electrochimica Acta

journal homepage: www.journals.elsevier.com/electrochimica-acta

Binder-free nanostructured germanium anode for high resilience lithium-ion battery

S. Fugattini [a,b,c,1,**], U. Gulzar [b,1], A. Andreoli [a,1], L. Carbone [b,*], M. Boschetti [a], P. Bernardoni [a], M. Gjestila [a], G. Mangherini [a], R. Camattari [a,f], T. Li [b], S. Monaco [b], M. Ricci [b], S. Liang [b], D. Giubertoni [c], G. Pepponi [c], P. Bellutti [c], M. Ferroni [d,e], L. Ortolani [e], V. Morandi [e], D. Vincenzi [a,*], R. Proietti Zaccaria [b,g,**]

[a] Physics and Earth Sciences Department via Saragat 1, University of Ferrara, Ferrara 44122, Italy
[b] Italian Institute of Technology, via Morego 30, Genova, GE 16163, Italy
[c] Bruno Kessler Foundation, via Sommarive, 18, Povo, TN 38123 Italy
[d] Department of Civil, Environmental, Architectural Engineering and Mathematics, University of Brescia - Via Valotti, 9-25123, Brescia, Italy
[e] CNR-IMM Bologna Section, Via Gobetti, 101, Bologna 40129, Italy
[f] National Institute of Nuclear Physics (INFN) - Section of Ferrara, via Saragat 1, Ferrara 44122, Italy
[g] Cixi Institute of Biomedical Engineering, Ningbo Institute of Materials Technology and Engineering, Chinese Academy of Sciences, Zhejiang 315201, PR China

ARTICLE INFO

Keywords:
Nanostructured germanium
Anode material
Lithium-ion battery
Plasma enhanced chemical vapor deposition
Binder-free

ABSTRACT

The development and the characterization of a nanostructured binder-free anode for lithium-ion batteries exploiting the germanium high theoretical specific capacity (1624 mAh g^{-1} for $Li_{22}Ge_5$ alloy) is herein presented. This anode secures remarkable performances in different working conditions attaining a 95% capacity retention at 1C (i.e., 1624 mA g^{-1}) after 1600 cycles at room temperature and a specific capacity of 1060 mAh g^{-1} at 10C and 450 mAh g^{-1} at 60C. The nanostructured binder-free germanium-based anode shows also strong resilience in terms of temperature tests, being it tested from -30 °C to +60 °C. Indeed, the specific capacity remains unaltered from room temperature up to +60 °C, while at 0 °C the cell is still retaining 85% of its room temperature capacity. In a full-cell configuration with $LiFePO_4$ as cathode, the Ge anode showed a stable specific capacity above 1300 mAh g^{-1} for 35 cycles at C/10. Concerning the fabrication procedure, a two-step realization process is applied, where a Plasma Enhanced Chemical vapor Deposition (PECVD) is employed to grow a germanium film on a molybdenum substrate followed by hydrofluoric acid (HF) electrochemical etching, the latter having the scope of nanostructuring the Ge film. Finally, compositional, morphological, and electrochemical characterizations are reported to fully investigate the properties of the binder-free nanostructured germanium anode here disclosed.

1. Introduction

The growing demand for portable power sources is currently making research on lithium-ion batteries (LIBs) a truly relevant topic. Since the first commercial device developed by Sony in 1991 [1], LIBs have been one of the cutting-edge technologies to store energy, employed in many fields such as portable devices, electric vehicles (EVs), electric grids, etc. The reliability of LIBs has allowed their use also in space applications such as satellites, spacecraft, rovers, orbiters, and astronaut equipment [2], replacing most of the previously adopted technologies, as recently occurred at the International Space Station (ISS) [3]. Nevertheless, the main challenge is still to develop batteries with enhanced specific capacity and energy density. The theoretical values of these quantities depend on the anode and cathode active materials, therefore researchers aim to find new kinds of electrodes [4,5] capable of overcoming the performances of the currently employed anodes [6] and cathodes [7].

* Corresponding authors.
** Corresponding authors at: Italian Institute of Technology, via Morego 30, Genova, GE 16163, Italy.
E-mail addresses: silvio.fugattini@gmail.com (S. Fugattini), Lorenzo.Carbone@lithium.plus (L. Carbone), monaco.simone@alice.it (S. Monaco), donato.vincenzi@unife.it (D. Vincenzi), remo.proietti@iit.it (R.P. Zaccaria).
[1] These authors contributed equally to this work.

https://doi.org/10.1016/j.electacta.2022.139832
Received 20 July 2021; Received in revised form 13 November 2021; Accepted 1 January 2022
Available online 4 January 2022

Furthermore, it is of paramount importance to verify the reliability of high-performance materials through long cycle tests in different temperature operating conditions, in order to ensure their applicability in some of the aforementioned applications. In fact, the required battery cycle life for EVs and low Earth orbit (LEO) satellites are respectively 2000–5000 [8] and 30,000–50,000 cycles [9], while the typical operating temperature range is -20 °C to +60 °C for EVs [8] and -20 °C to +40 °C for planetary rover and lander energy storage systems [9,10].

Li-alloying materials [6,11] — and in particular Group IV-A elements including silicon (Si), germanium (Ge), and tin (Sn) — are considered promising anodic candidates for the next generation of LIBs [12]. Compared to the conventional graphite anode, which has a theoretical specific capacity of 372 mAh g^{-1}, these alloying materials provide theoretical specific capacities of 4200 mAh g^{-1} [13–15], 1624 mAh g^{-1} [16–18], and 994 mAh g^{-1} [19,20] when lithiated up to $Li_{22}Si_5$, $Li_{22}Ge_5$, and $Li_{22}Sn_5$ phases, respectively. Ge is characterized by remarkable properties in terms of intrinsic electrical conductivity and lithium ion diffusivity, respectively 10,000 times [21] and 400 times [22] higher than Si, hence making Ge an excellent candidate for high performance batteries. Furthermore, the isotropic lithiation of Ge can better accommodate, with respect to Si, the occurrence of large volumetric variations (~ 250–300% for Ge,~ 400% for Si [23]) during lithiation/de-lithiation processes. Indeed, with Ge is possible to achieve the reversible formation of a nano-porous network during the alloying processes, allowing an easy relaxation of the stress [24] and an additional structural stability leading to the formation of a mechanically robust solid electrolyte interphase (SEI) [25,26].

Therefore, several compliant Ge structures including micro/nanoparticles [22,27,28], nanowires [29,30], nanotubes [31],and microcubes [32] have been studied in literature to reversibly address these massive volumetric expansions in order to improve the cycle life of the active material. However, most of these strategies involve the use of inactive materials, such as binders and conductive agents [33] to ensure the mechanical stability of the active material and enhance the electrical conductivity [34], hence determining an energy density decrease of the whole battery system [35]. Conversely, direct growth of binder-free Ge nanostructures positively addresses this aspect by realizing anode materials with consequential higher specific capacity, assuring also a large electrode/electrolyte contact area and a fast lithium ion transport [36,37]. In this respect, many authors reported bottom-up Ge structures such as nanowires (NWs) obtained via a simple thermal Ge/Sn co-evaporation method on Au-catalyzed low-temperature substrates [36] or Sn seeded Ge NWs on a stainless steel current collector via a solvent vapor growth (SVG) system [38,39].

Herein, a two-step method to produce a binder-free Ge anode is presented, combining the use of a high deposition-rate technique with a common top-down approach to nanostructure semiconductor films. The novelty of this process consists in depositing Ge on metallic substrates by means of Plasma Enhanced Chemical Vapor Deposition (PECVD) and subsequently performing an electrochemical etching with hydrofluoric acid (HF) to create the final nanostructure. The Ge anode for LIBs realized following this procedure was capable of 95% capacity retention after 1600 cycles at 1C current rate in room temperature conditions (RT, 20 °C), with a coulombic efficiency higher than 99.5%. Furthermore, the anode showed a specific capacity as high as 1060 mAh g^{-1} and 450 mAh g^{-1} when tested at 10C and 60C, respectively (1C=1624 mA g^{-1}). The binder-free Ge anode was also tested in a wide range of working temperatures without observing any capacity fade when cycling at high temperatures (up to +60 °C), while at 0 °C it was still retaining 85% of its RT capacity. Finally, the Ge anode attained a stable specific capacity above 1300 mAh g^{-1} for 35 cycles at C/10 in a full-cell using $LiFePO_4$ as the positive electrode. A deep study of this Ge-based anode was carried out, through morphological and compositional characterization of the as-prepared anode as well as its electrochemical and post-mortem analysis.

2. Materials and methods

2.1. Plasma enhanced chemical vapor deposition (PECVD)

The first step in the anode realization consisted in the Ge film deposition by means of the PECVD technique [40]. PECVD is a deposition technology extensively used in semiconductor industry to fabricate integrated circuits as well as photovoltaic, photonic, optical and biomedical devices being it capable of reaching higher deposition rates (up to 10 nm s^{-1}) than other deposition techniques [41].

To ensure electrical conductivity inside the battery prototypes, Ge growth occurred on a metallic substrate acting as current collector. The choice of the metal depended on several factors. Firstly, the metal had to be characterized by a high melting temperature and a low vapor pressure in order to prevent any contamination of the PECVD chamber, therefore making this process compatible with standard semiconductor fabrication facilities. In fact, the environment inside the PECVD reactor is critical due to the low base pressure (10^{-8} mbar) and the high process temperature (above 400 °C). Secondly, the metallic substrate had to be resistant to HF, due to the required after deposition HF electrochemical process on Ge. Based on these motivations, molybdenum (Mo) was identified as the metal of choice over the more common copper and nickel typically employed by the battery industry [35]. In this respect, 25 μm-thick Mo foils (Sigma-Aldrich, purity higher than 99.9%) were sequentially rinsed in dichloromethane (CARLO ERBA Reagents, RPE grade), acetone (CARLO ERBA Reagents, purity $\geq$ 99.5%), 2-propanol (Sigma-Aldrich, purity $\geq$ 99.8%) and de-ionized water to remove any impurity. Afterwards, they were outgassed at 200 °C for 20 min inside the load-lock of the PECVD equipment at a pressure around 2×10^{-6} mbar. Finally, the samples were placed inside the process chamber by means of a manipulator and heated again above 400 °C. A plasma was ignited using H_2 as carrier gas and the deposition occurred exploiting GeH_4 as precursor gas at a pressure around 10^{-3} mbar, resulting in a growth rate of 1.26 nm s^{-1}. No binder was needed to improve the adhesion between the substrate and the Ge film, whose thickness was verified through Secondary Ion Mass Spectrometry (SIMS) depth profiles.

2.2. Hydrofluoric acid (HF) electrochemical etching

To withstand the volume variations experienced by Ge during charge/discharge cycles, many authors have employed bottom-up techniques to realize Ge compliant matrices [30,36–38,42]. Here, a top-down process based on HF electrochemical etching was chosen to create nanostructured Ge [43,44]. In particular, a custom made PTFE (PolyTetraFluoroEthylene) single-tank electrochemical cell was used for this purpose [45]. Specifically, a graphite rod (Alfa Aesar 040765, 99.9995% purity) acting as a counter electrode was immersed in a solution composed by HF (CARLO ERBA Reagents, 50% diluted, MOS grade) and ethanol (CARLO ERBA Reagents, RS grade) (3:1 v/v), while the backside of the sample was pressed on an aluminium plate to ensure the electrical contact. Assuming a tetravalent dissolution model for Ge [46–48], 70% of the Ge mass was expected to be removed by means of a 40 mA current flowing for 180 s. The result was the formation of a nanostructured morphology, namely the aforementioned approach avoided the homogeneous dissolution of the entire Ge layer.

2.3. Li-ion half-cell assembly and disassembly

The binder-free Ge anode realized according to the two-step process previously described was cut into a 15 mm diameter disk and tested in CR2032 coin cells assembled inside an Argon-filled MBraun glovebox with H_2O and O_2 levels below 0.1 ppm. The electrode mass loading ranged from 0.22 to 0.30 mg and its composition was 100% active material, as neither binder nor conductive agents were employed. The anode was coupled with a metallic lithium chip as counter electrode

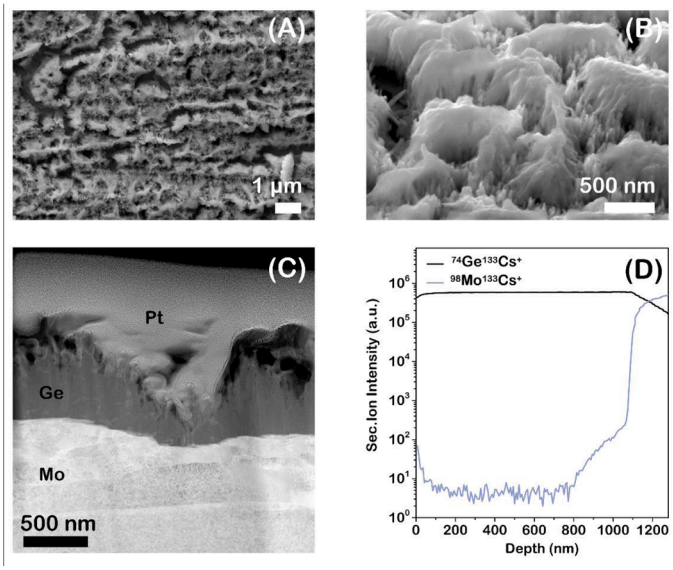

Fig. 1. Top-view (A) and tilted (B) SEM images of the nanostructured Ge film. TEM image (C) of the cross-sectional specimen, Ge and Mo SIMS depth profiles (D) of the as-deposited film.

(diameter 15.6 mm × 0.45 mm thickness; MTI Corporations), thus obtaining a half-cell. A dried glass fibre separator (Whatman GF/D) was soaked with 200 µL of freshly prepared electrolyte composed by 1M lithium hexafluorophosphate ($LiPF_6$) dissolved in 1:1 mixture of ethylene carbonate (EC) and dimethyl carbonate (DMC) (LP30 [49], Sigma-Aldrich) with 10% v/v fluoroethylene carbonate (FEC, Sigma-Aldrich) as additive [50–52].

Post-mortem analyses were carried out after stopping the cycling protocol at 1.5 V, in order to de-lithiate the active material. The cell was disassembled in the same glovebox used for the assembly, rinsed with DMC (Sigma-Aldrich, anhydrous purity ≥ 99%) and dried under vacuum overnight.

2.4. Cathode preparation and full-cell assembly

The Ge anode performance was assessed also in full-cell configuration by coupling the negative electrode with one of the most common cathode materials, $LiFePO_4$ (LFP, Nanomyte BE-60E-NEI corporation) using 200 µl of 1M $LiPF_6$ in EC:DMC (1:1) + 10% v/v FEC as electrolyte. The slurry, cast on an aluminum foil, was composed by 80% LFP, 10% PVDF, and 10% SuperP (Alfa Aesar: 99+% metal basis). Before the assembly, the anode was pre-lithiated as described in Ref. [53] in order to avoid lithium losses during the first cycle. The full-cell balance was designed to achieve an anode/cathode capacity ratio of 1.01. Therefore, the active mass loading of the cathode was 3.26 mg resulting in a cell with a theoretical capacity of 0.55 mAh and an overall theoretical specific capacity of 154 mAh g^{-1}, considering both anode and cathode active masses.

2.5. Characterization techniques

The thickness of the Ge film was verified through a Secondary Ion Mass Spectrometry (SIMS) analysis. SIMS was carried out in MCs^+ mode, i.e. using 3 keV impact energy Cs^+ as primary ions and collecting the positive secondary ions formed by both the atoms of interest and the re-sputtered Cs^+ ions [54] (Cameca SC-Ultra). In this regard, the Ge erosion rate was determined by using a reference sample consisting in a PECVD-deposited Ge film on a Si wafer, in order to have a Ge film on a flat surface with the same density of the ones deposited on Mo substrates. The need of the reference sample was motivated by the pronounced roughness and scarce planarity of the Mo substrate, which did not allow for an accurate measurement of the crater depths by mechanical stylus profilometer directly conducted on Ge-Mo structure. Furthermore, in order to reduce the impact of the Ge surface roughness on the SIMS depth resolution, the sample holder was mounted on a rotating stage [55] with the axis of rotation normal to the sample surface and aligned to the coincidence point of primary and secondary ion beams.

Scanning Electron Microscopy (SEM) characterization was performed using a Jeol JSM7401F instrument. The samples were conventionally mounted on a holder with a conductive carbon tape. Secondary Electrons (SE) images were acquired using 15 keV accelerating voltage and 10 µA beam current.

Transmission Electron Microscopy (TEM) was carried out by means of the FEI Tecnai F20 ST microscope. To investigate the nanostructure of the Ge layer, a cross-sectional specimen was prepared by a dual beam SEM-FIB (Focused Ion Beam) Zeiss CrossBeam 340, using a conventional approach for the fabrication of a cross-sectional thin lamella and starting from the deposition at the sample surface of a platinum protective layer.

X-ray diffraction (XRD) analysis was carried out on a Malvern PANalytical Empyrean X-ray powder diffractometer equipped with a 1.8 kW CuKα ceramic X-ray tube, PIXcel^{3D}2 × 2 area detector and operating at 45 kV and 40 mA. The diffraction pattern was collected in air, at room temperature, using Parallel-Beam (PB) geometry and symmetric reflection mode.

X-ray photoelectron spectroscopy (XPS) was performed with a Kratos Axis Ultra DLD spectrometer equipped with a monochromatic Al Kα source (15 kV, 20 mA).

2.6. Electrochemical tests

The electrochemical properties of the Ge anode were investigated with a Bio-Logic BCS-805 multichannel battery unit controlled by BT Lab V1.30.

Cyclic voltammetry (CV) tests were carried out on 2032 coin half-cells assembled with the binder-free Ge anode and tested at 0.1 mV s^{-1} in the 0.01–1.5 V voltage range, while half-cells containing a pristine Mo disk as anode (Fig. S1) were tested at 0.1 mV s^{-1} in the voltage range between 0.01 and 2.8 V.

Galvanostatic cycling tests were performed with 2032 coin half-cells in the 0.01–1.5 V voltage range. These tests started with three cycles at C/10 current rate (1C = 1624 mA g^{-1}), subsequently named activation cycles, to ensure the formation of a good and stable SEI layer at RT [56, 57]. The rate capability test was performed by changing the current rate every 10 cycles from C/10 (162 mA g^{-1}) up to 60C (97,440 mA g^{-1}) before going back to C/10. Long cycling tests at a constant current of 1C were carried out at RT, at 0 °C, at −10 °C, and by varying the temperature range every 10 cycles from RT down to -30 °C, then raising it up to +60 °C and lowered again down to RT.

The full-cells were characterized through galvanostatic charge/discharge cycles at C/10 at RT in the voltage window 2.5–4.2 V, calibrating the C-rate according to the cathode active mass loading (1C = 170 mA g^{-1}).

Electrochemical Impedance Spectroscopy (EIS) was performed in the frequency range 0.1 Hz–10 kHz with a signal amplitude of 10 mV when the electrode was in a de-lithiated state. Nyquist plots were analysed using a nonlinear least square (NLLS) fit [58] to evaluate the total and the electrolyte resistance applying the equivalent circuit R(RQ)(RQ)Q, where R is a resistance and Q a constant phase element (CPE) [59] as discussed below. These analyses were carried out using Boukamp software [60] and only the results having a chi-square (χ^2) lower than 10^{-4} were accepted.

An OXFORD cryostat CCC1204 coupled with a liquid helium compressor Cryodrive 1.5 was employed to carry out the galvanostatic measurements in the selected range of temperatures (-30 °C to +60 °C). The cryostat is composed by a heater and a cold head both managed by a temperature controller (TC) through a Proportional-Integrative-

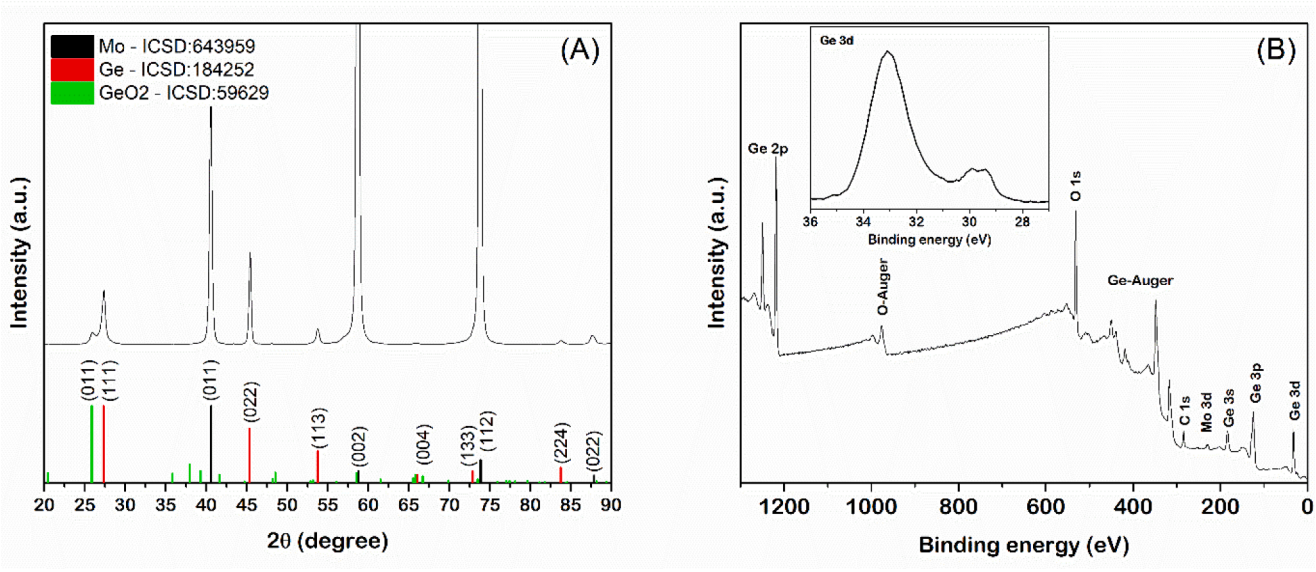

Fig. 2. XRD pattern (A) and XPS wide survey (B) of the nanostructured Ge film. The inset in (B) reports the magnification of the Ge 3d peak.

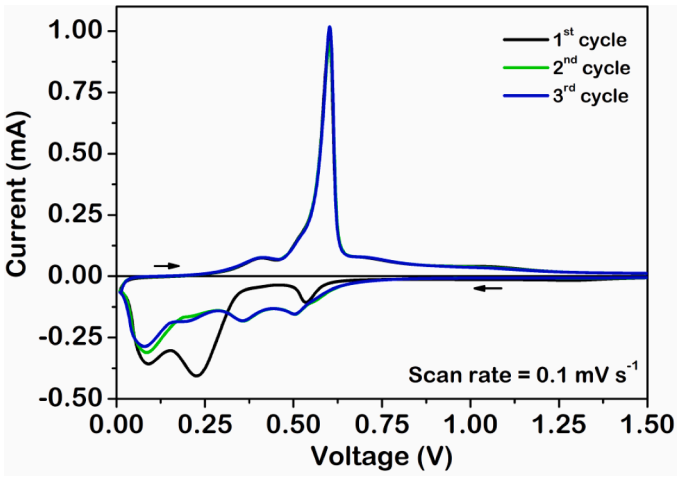

Fig. 3. Cyclic voltammetry of the nanostructured Ge anode performed at 0.1 mV s^{-1} in the voltage range 0.01–1.5 V. The CV starts from 1.5 V and follows the direction indicated by the arrows.

Derivative system (PID). The sample chamber, surrounded by a high vacuum external chamber ensuring thermal isolation, was filled with argon to avoid any internal condensation. A printed circuit board (PCB) was specifically designed to host a coin-cell 2032 and to connect wirings needed for the electrochemical tests with the Bio-Logic BCS-805 multi-channel battery unit (Fig. S2). The PCB had also a temperature sensor (Pt1000, Heraeus 32207615 Class B) to guarantee an alternative way—with respect to the TC—to monitor the cell temperature, whose value was read by means of a dedicated controller (ATR 121, Pixsys electronics). Importantly, through all the measurements, full readings agreement was registered between the two temperature sensors. Finally, Electrochemical Impedance Spectroscopy (EIS) tests were performed at each temperature step in order to evaluate the achievement of thermal equilibrium inside the cell.

3. Results and discussion

3.1. Structural and morphological characterizations

Fig. 1 shows the Ge layer after the HF porosization treatment. The top- (Fig. 1A) and tilted-view (Fig. 1B) highlight a morphology on the Ge surface characterized by vertical structures made of ridges and valleys. The width of the single ridge ranges between 100 and 300 nm as shown

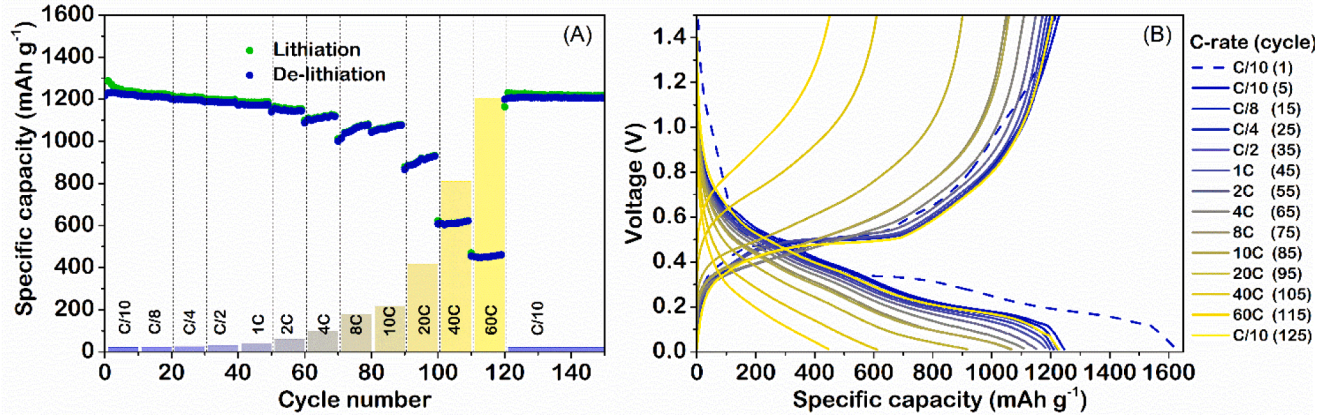

Fig. 4. Rate capability (A) and charge/discharge profiles (B) of the nanostructured Ge anode performed at various C-rates (from C/10 up to 60C) in the 0.01–1.5 V voltage range, changing the current rate every 10 cycles. The dashed line in (B) is the first charge/discharge profile.

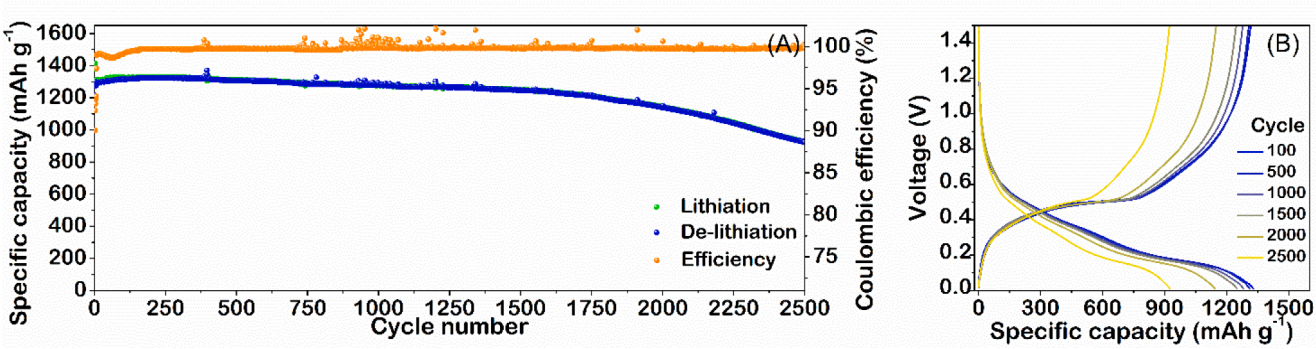

Fig. 5. Long cycling behavior (A) and charge/discharge profiles (B) of the nanostructured Ge anode at the current rate of 1C in the 0.01–1.5 V voltage range.

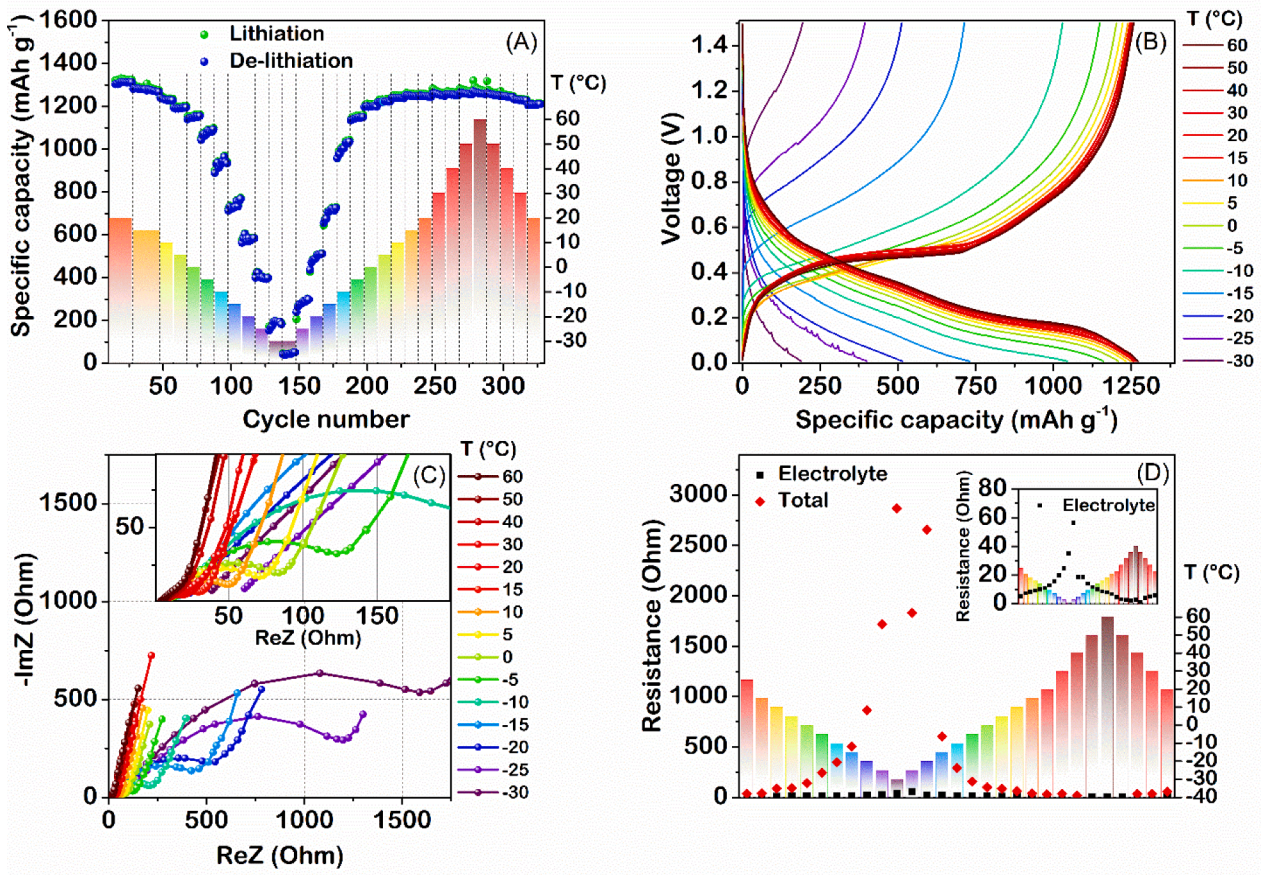

Fig. 6. Specific capacity versus cycle number (A) and charge/discharge profiles (B) of the nanostructured Ge anode performed at the current rate of 1C. The bars in (A) and (D) represent the temperature at which each cycle is performed that varies every 10 cycles from RT to -30 °C, heating up to +60 °C and finally back to RT. In (C) Nyquist plots of the impedance spectroscopy tests performed every temperature step in the 0.1 Hz–10 kHz frequency range. Electrolyte and total resistance values are extrapolated fitting the Nyquist plots and represented versus the temperature (D).

in Fig. 1B. The TEM image of Fig. 1C reports the cross-sectional view of the anode, where it can be clearly distinguished the Mo substrate located at the bottom of the Ge layer. The platinum layer is added as protection to prevent any possible modification of the surface morphology during the cross-sectional specimen fabrication. This perspective confirms that the HF etching thins the Ge film in some regions —previously named as valleys— and at the same time creates a nanometric structure on the surface of the whole Ge film. Vice-versa, the bottom part of the Ge layer is compact and dense, assuring a good and stable adhesion to the Mo substrate. Furthermore, the sharp interface between Ge and Mo indicates that there is no modification in the structure or in the local composition of the Ge layer. Fig. 1D reports the SIMS depth-profiling of the as-deposited Ge film, carried out taking into account the Ge and Mo elemental distributions of a 500 × 500 μm^2 sample area. Starting from the Ge external surface (depth = 0 nm), the intensities of Mo and Ge secondary ions are reported as a function of the depth in order to evaluate the thickness of the Ge film through the half maximum value of the $^{98}Mo^{133}Cs^+$ signal. After the initial 800 nm, where the Ge secondary ions are the most abundant element detected, a first increasing slope of the Mo signal is observed in the SIMS profile up to 1050 nm, a behavior possibly ascribed to the formation of an inter-diffusion layer between Mo and Ge. However, Fig. 1C underlines a wavy and rough surface of the Mo substrate that may be responsible for the behavior of the SIMS profile until 1050 nm. Between 1050 nm and 1100 nm, a second increasing

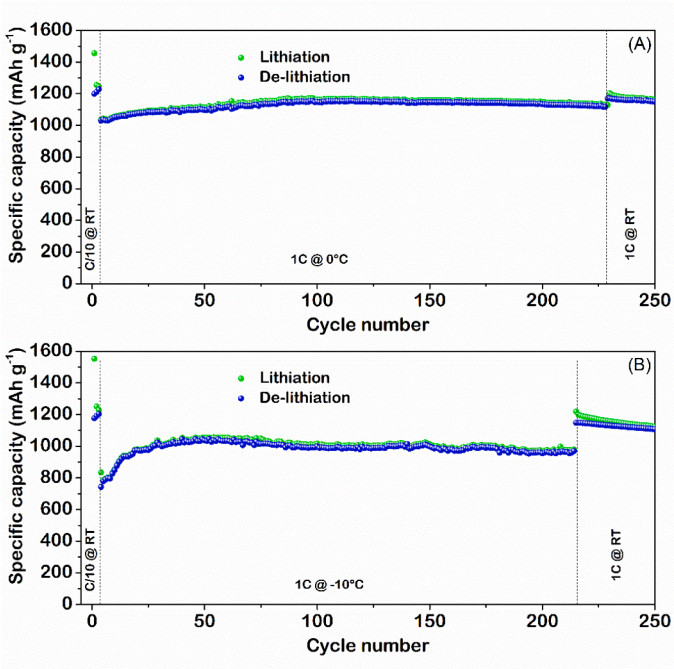

Fig. 7. Long cycling behavior of the nanostructured Ge anode at the current rate of 1C in the 0.01–1.5 V voltage range at 0 °C (A) and -10 °C (B).

rapid slope of the $^{98}Mo^{133}Cs^{+}$signal is observed followed by an intensity flattening together with a slow decrease of the $^{74}Ge^{133}Cs^{+}$signal starting around 1100 nm. These readings define an average thickness of the Ge film at about 1100 ± 50 nm. The comparison between this result and the Ge layer cross-section in Fig. 1C indicates that the HF etching reduced the overall Ge thickness in a dishomogeneous way, thus creating the nanostructured morphology depicted in Fig. 1A,B.

Fig. 2A reports the XRD pattern of the nanostructured anode that confirms the presence of the cubic Ge phase (ICSD:184252) and of the hexagonal GeO_2 phase (ICSD:59629), the latter ascribed to a partial sample oxidation. As expected, apart from the Mo metallic substrate (cubic phase, ICSD:643959), no other crystalline phases were revealed. Fig. 2B shows the XPS wide survey of the nanostructured anode to investigate the superficial composition of the electrode. This analysis is in line with the results of the XRD pattern, as no other noteworthy element apart from Ge was detected. The inset reports the Ge 3d core level to highlight the presence of the Ge-O bond peak at 32.9 eV and the Ge-Ge bond peak at 29.3 eV [61], confirming a partial oxidation of the sample surface. It is also observed a low intensity peak attributed to the Mo 3d shell, which could be ascribed to the complete erosion in some areas of the Ge film during the HF etching treatment.

3.2. *Electrochemical characterizations*

The electrochemical characterizations of the Ge-based anode are carried out using 2032 coin-cells. Cyclic voltammetry (CV) tests are performed in the voltage range between 0.01 V and 1.5 V at the scan rate of 0.1 mV s^{-1}, as shown in Fig. 3. Moreover, since Mo and Mo-oxides (MoO_2 and MoO_3) are among the Li^{+}insertion compounds [62–66], a CV test is performed on the bare Mo substrate to confirm that Mo does not play any role as active material (see Fig. S1).

The first cycle of the Ge anode CV test reported in Fig. 3 reveals three peaks in the cathodic region at 0.53 V, 0.23 V, and 0.09 V that could be ascribed to the SEI and Ge alloys formation, as previously reported by the authors [22]. Indeed, the subsequent cycles show the formation of multiple peaks between 0.50 V and 0.08 V, which are associated to the multistep lithiation process of Ge [67]. The anodic region of the CV test reveals instead only two peaks for all cycles, a broad peak at 0.41 V and a sharp one at 0.6 V, both related to the de-lithiation reactions of the active material [30]. Therefore, all the galvanostatic tests of the half-cells containing the Ge-based anode are carried out in the 0.01–1.5 V voltage range and start with an activation procedure based on three cycles at C/10 current rate, to ensure the formation of a good and stable SEI layer at RT [56,57,68] as suggested from the difference between the first and second cycle of the cyclic voltammetry test of Fig. 3.

The specific capacity behavior and voltage profiles concerning the rate capability test of the binder-free Ge anode are shown in Fig. 4A and Fig. 4B, respectively. This test consists in increasing the current rate every 10 cycles from C/10 to 60C and then reducing it down to C/10 to evaluate the anode capability to recover its own original performance. The capacity behavior of the Ge anode reveals an irreversible capacity during the first cycle—represented by the dashed lines in Fig. 4B—attributed to the SEI layer formation [68]. At low C-rates, the cell shows a specific capacity of 1250 mAh g^{-1} with a negligible fading up to 1C, hence demonstrating a good anode performance at these regimes. When the measurement is shifted to current rates higher than 1C, it is observed –as expected– a further capacity reduction, down to 1150 mAh g^{-1}, 1110 mAh g^{-1}, and 1080 mAh g^{-1} for 2C, 4C, and 8C, respectively. Up to 10C the polarization associated to the voltage profiles shown in Fig. 4B is modest and the anode is still releasing 1060 mAh g^{-1}. At higher current rates the growth of the polarization effect causes a reduction of the capacity to 900 mAh g^{-1}, 600 mAh g^{-1}, and 450 mAh g^{-1} at 20C, 40C, and 60C, respectively. Nevertheless, this capacity drop is not due to a loss of active material as the cell regains its initial capacity once the current is lowered back to C/10 and any polarization effect disappears.

The aging of the Ge nanostructure is investigated by performing galvanostatic measurements at the current rate of 1C. Three coin-cells are stopped after the 1st, the 30th and the 500th cycle, disassembled in the de-lithiated state and observed at the SEM to determine the morphology evolution after multiple lithiation/de-lithiation processes (Fig. S3). The SEM image related to the end of the first cycle reveals the already discussed vertically oriented morphology of the Ge anode with an increased average width of the Ge structures of about 1 μm. The latter morphology sheds light on the structural rearrangement of the active material after the first activation cycle. Indeed, as discussed in relation to the first cycle of the CV test, Fig. 3 reveals the formation of multiple peaks during the lithiation processes ascribed to the formation of the SEI on the electrode surface. Therefore, the growth of the as prepared Ge structures from 100 to 300 nm (see Fig. 1A,B) to 1 μm after one cycle, may be related both to the formation of a passivation film on the active material surface and its first lithiation. A similar morphology is also observed in the SEM image collected after 30 cycles, hence confirming the formation of a stable SEI. The last post-mortem image obtained after 500 cycles shows instead a sensibly increased width of the Ge structures, possibly resulting from their merging during the lithiation/de-lithiation processes. To further investigate the reliability of the anode a prolonged cycling test at constant current rate of 1C is performed, as shown in Fig. 5.

The galvanostatic cycling test of the binder-free Ge anode reported in Fig. 5A and performed in the voltage range between 0.01 V and 1.5 V at the current rate of 1C (1624 mA g^{-1}), delivers a specific capacity higher than 1300 mAh g^{-1} with a coulombic efficiency of 99.6% for more than 1000 cycles. The capacity retention is 95%, 87%, and 71% after 1600, 2000, and 2500 cycles, respectively. This capacity fading may be ascribed to the progressive loss of active surface of the Ge anode, as testified by the progressive shortening of the voltage profile plateaus (Fig. 5B). Indeed, as already discussed in the aging analysis of Fig. S3, the morphological rearrangement of the Ge structure during several charge/discharge processes reveals the production of agglomerates with increasing size upon cycling, which may lead to a possible loss of active surface area that no longer contribute to the electrochemical process. The voltage profiles in Fig. 5B summarize the characteristic

Table 1
Performance comparison of Ge-based anode materials from literature.

Material	Preparation method	Specific capacity [mAh g^{-1}] (low C-rate)	Specific capacity [mAh g^{-1}] (high C-rate)	Overall number of cycles (C-rate, spec. cap. [mAh g^{-1}])	Mass loading [mg] (mass density [mg/cm^2])	Ge content [%]	Voltage range [V]	Refs.
Nanostructured Ge film	PECVD + HF etching	1250 (0.1C)	450 (60C)	2500 (1C, 925)	0.2–0.3 (0.11–0.17)	100	0.01–1.5	This work
Sn-seeded nanowires	Vapor-Liquid-Solid (VLS) technique	1250 (0.1C)	722 (2C)	1100 (0.5C, 888)	—	83 (5:1 ratio Ge:Sn)	0.01–1.5	[38]
Amorphous Ge films	Physical vapor Deposition (PVD)	1700 (C/4)	500 (1000C charge, 1C discharge)	60 (C/4, 1700)	0.042 (–)	100	0–1.5	[73]
Ge grains	Thermal reduction of GeO_2	1500 (C/30)	1100 (0.5C)	40 (0.5C, 1100)	–	–	0.02–2.0	[27]
Ge nanowires	Thermal co-evaporation method	–	900 (1C)	50 (1C, 900)	–	–	0–1.2	[36]
Ge nanowires	VLS technique	1141 (C/20)	600 (2C)	50 (rate cap., 600)	1 (–)	~ 100	0–2.5	[37]
Ge nanowires	Vapor -solid-solid mechanism	1318 (0.1C)	1081 (2C)	1900 (1C, 866)	– −0.19	~ 100	0.01–1.5	[39]
Ge nanowires in graphite tubes	CVD system	1310 (C/6)	232 (6C)	110 (rate cap., 1300)	0.5 (–)	70 (Ge-graphite)	0.005–1.2	[29]
Ge nanowires	VLS technique	1405 (0.1C)	1200 (5C)	100 (rate cap., 1200)	0.12–0.86 (–)	~ 100	0.01–2.0	[30]
Ge nanotubes	Kirkendall effect	1022 (0.2C)	580 (20C)	50 (0.2C, 1002)	–	–	0–1.5	[31]
Ge microcubes	Hydrogen reduction method	1250 (0.1C)	1121 (50C charge, 1C discharge)	500 (1C, 1204)	– (~ 2)	100	0.005–1.5	[32]
Ge/SWCNT paper (34% Ge)	Ge particles deposited on SWCNT	750 (0.015C)	–	40 (0.015C, 417)	–	–	0.01–2.0	[17]
Micro sized porous Ge particles	Reduction of GeO_2	1100 (0.6C)	437 (10C)	1800 (5C, 469)	– (0.56–1)	70	0.02–1.2	[74]
Ge micro particles	Halogen-free process	600 (1C)	200 (10C)	25 (1C, 580)	0.5–1 (–)	–	0.05–1.5	[75]
Ge/Co_3O_4 nano-rod array	Electron beam evaporation	1237 (0.5C)	675 (20C)	600 (10C, 1018)	– −0.19	100	0.02–1.0	[76]
Ge nanoparticles	Chemical de-alloying process	1191 (0.1C)	767 (1C)	210 (rate cap., 1200)	–	–	0.05–0.9	[77]
Mesoporous Germanium	Mechanochemical reaction	950 (0.1C)	–	20 (0.1C, 789)	–	–	0–1.5	[78]
Ge powder	Commercial Ge powder	1152 (1C)	700 (10C)	2500 (variable C-rates, 1152)	– (0.3–0.5)	40	0–1.0	[79]

electrochemical behavior of the Li-Ge reactions, with a multi-step reaction during the discharge processes from 0.6 V to 0.3 V and a long plateau at 0.2 V. The charge processes are instead characterized by the plateau at about 0.5 V followed by step reactions up to 1.2 V. Finally, the Ge anode exhibits a negligible polarization for the first 2000 cycles accompanied by a remarkable specific capacity.

In order to evaluate the resilience of the Ge anode, temperature tests are performed choosing harsh scenarios such as the NASA requirements for planetary rovers and landers [10,69]. Following the activation cycles at RT, galvanostatic tests at 1C are then carried out by varying the temperature every 10 cycles from RT down to -30 °C, then up to +60 °C, to finally go back to RT. Fig. 6A shows the specific capacity vs. cycle number trend while the colored bars define the cycling temperature. The Ge anode specific capacity is initially higher than 1300 mAh g^{-1} then exhibits a slight decay upon temperature decrease, losing nearly 4% every 5 °C. At 0 °C it reaches about 1100 mAh g^{-1} retaining around 85% of the initial capacity. When going further down in temperature, it is observed an increasing dropping rate of the specific capacity until reaching 200 mAh g^{-1} at -30 °C. Interestingly, the specific capacity recovery observed increasing the temperature, is slightly faster than the capacity fading along the cooling region, delivering a specific capacity of about 1200 mAh g^{-1} at 0 °C. When the RT is reached again, a specific capacity of about 1300 mAh g^{-1} is measured, with a stable trend up to +60 °C. Fig. 6B depicts the charge/discharge profiles vs. temperature at the current rate of 1C. The voltage profiles recorded at temperature higher than -15 °C show the typical shape of the Li-Ge electrochemical reactions, revealing the complete evolution of the charge/discharge processes. However, the cell polarization increases throughout the temperature decrease region reflecting the capacity fading of Fig. 6A and revealing the hindering effect of low temperature on the electrochemical performance of the Ge anode. In order to provide further insights about the underneath motivations related to the remarkable performance demonstrated by the Ge anode, electrochemical impedance spectroscopy (EIS) is performed. In particular, Fig. 6C shows the Nyquist plots collected between -30 °C and +60 °C. The plots reveal the typical depressed semicircles related to both the SEI formation and the charge transfer element, with overall values varying of about three orders of magnitude in the -30 °C to +60 °C temperature range. Indeed, the resistance values are calculated through the NLLS fit analysis [58] of the EIS spectra using as equivalent circuit $R_e(RQ)_{SEI}(R_{CT}Q_{DL})Q$, where R_e is the electrolyte resistance, $(RQ)_{SEI}$ is the element referred to the passivation film on the electrode surface, R_{CT} is the charge transfer resistance related to the lithiation/de-lithiation processes, Q_{DL} is the double layer capacitance, and Q is related to the Li^+ diffusion in the electrode. However, in order to compare the data at each temperature, the resistance shown in Fig. 6D is the sum of all resistances. The cell total resistance shows a slight increase up to 150 Ω while the temperature decreases down to -5 °C, reflecting the stable voltage profile of Fig. 6B and confirming the anode stability in this temperature region. However, the cooling down until -30 °C triggers a fast resistance increase of about 3000 Ω, mainly ascribed to the resistivity variations experienced by the Ge with the temperature variation [70]. Moreover, the R_e depicted in the inset of Fig. 6D reveals a comparable trend with respect to the total resistance of the cell, with the maximum resistance value at -30 °C of about 60 Ω, which may partially contribute to the enhanced polarization effect noticed in the charge/discharge profiles (Fig. 6B) hindering the electrochemical reactions and being partially responsible for the capacity fading at low T.

The real use of the Ge anode at low temperatures is investigated through long charge/discharge tests at 0 °C and -10 °C whose cycling behavior is shown in Fig. 7 and the corresponding voltage profiles in Fig. S4. After the initial activation cycles the cell temperature is kept at the desired values for more than 200 cycles, when it is raised again at RT. At both temperatures the Ge anode is able to show stable performances with a capacity of 1150 mAh g^{-1} at 0 °C and 1000 mAh g^{-1} at -10 °C before regaining the initial value once the temperature is restored at RT. The voltage profiles (Fig. S4) show no polarization effect testifying that the Ge anode is still reliable in these working conditions.

Finally, the use of the nanostructured Ge film as anode in LIBs is assessed in a full-cell containing $LiFePO_4$ as cathode active material. The battery is cycled at C/10 in the voltage range 2.5–4.2 V at room temperature. After exhibiting an 86% coulombic efficiency during the first cycle, the Ge anode releases a specific capacity higher than 1300 mAh g^{-1} (Fig. S5A), performance in line with the results shown in the half-cells (Figs. 4,5). The voltage profiles (Fig. S5B) show a plateau around 3.4 V, which is typical of the LFP cathode [71] thus confirming the stability of the Ge anode/LFP cathode system through cycling, whose overall specific capacity is 126 mAh g^{-1} considering both anode and cathode active masses.

The Ge anode here presented shows performances that can be considered surely remarkable when compared to the state of the art. Table 1 reports a brief summary of some of the most relevant Ge-based anodes found in literature, considering the specific capacity achieved at low and high C-rates and the overall number of cycles. The voltage range and the anode mass loading—when explicitly reported—are listed as well, in order to ease the comparison [72]. Temperature tests are instead not mentioned in the comparison as they were not discussed by the authors of the cited papers, which performed electrochemical tests only at RT. From Table 1 it can be easily concluded that the Ge anode presented in this work exhibits a specific capacity at low C-rates that is in line with other works, while owns a better performance in terms of highest investigated C-rate (60C, 450 mAh g^{-1}) and number of overall cycles (2500) carried out.

4. Conclusion

In this work, a highly resilient nanostructured Ge anode for high-performance LIBs is introduced. The synthesis procedure is based on a two-step realization process that allows the production of a binder-free anode material capable to reach a 95% capacity retention after 1600 cycles at 1C. The electrochemical performance of the conceived Ge anode was evaluated through galvanostatic cycling tests, revealing a stable behavior in the full range of the investigated C-rates (from C/10 to 60C) with 1060 mAh g^{-1} at 10C and 450 mAh g^{-1} at 60C. Furthermore, temperature tests were also performed, showing the remarkable capability of the Ge-based anode to recover the initial RT capacity after 350 cycles performed by cooling the cell down to -30 °C and by heating it up to +60 °C. In terms of cycling stability, prolonged galvanostatic tests at 1C current rate at 0 °C (1150 mAh g^{-1}) and -10 °C (1000 mAh g^{-1}) were carried out, verifying the use of the Ge anode in these conditions. The Ge anode performances were confirmed in a full-cell using $LiFePO_4$ as the positive electrode, maintaining a stable specific capacity above 1300 mAh g^{-1} for 35 cycles at C/10. All in all, the presented results demonstrate how the herein developed Ge-based anode could indeed play an important role for high performance batteries.

Declaration of Competing Interest

The authors declare no conflict of interest.

Acknowledgments

This work was supported and financed by the Italian Space Agency (ASI) in the frame of the ANGELS (ANodi in GErmanio nanoporoso per batterie al Litio per applicazioni aeroSpaziali) and GLITTERY (Germanium Lithium Ion baTTERY) projects (grant numbers ASI_n._2018-1-U.0 and ASI_n._2021-2-U.0, respectively). We would like to thank Dr. S. Marras and Dr. M. Prato for providing XRD and XPS characterization respectively. The help and support of M. Brunori during the writing of the manuscript is gratefully acknowledged.

Supplementary materials

Supplementary material associated with this article can be found, in the online version, at doi:10.1016/j.electacta.2022.139832.

References

[1] J.D. Ocon, J.K. Lee, J. Lee, High energy density germanium anodes for next generation lithium ion batteries, Appl. Chem. Eng. 25 (2014) 1–13, https://doi.org/10.14478/ace.2014.1008.

[2] T. Ormston, V.D. Tran, M. Denis, N. Mardle, L. Lucas, L. Maleville, K. Van Der Pols, Lithium ion battery management strategies for european space operations centre missions, in: Proceedings of the 13th International Conference on Space Operations, SpaceOps, 2014, p. 2014, https://doi.org/10.2514/6.2014-1883.

[3] E. Schwanbeck, P. Dalton, International space station lithium-ion batteries for primary electric power system, in: Proceedings of the European Space Power Conference (ESPC), IEEE, Juan-les-PinsFrance, 2019, p. 1, https://doi.org/10.1109/ESPC.2019.8932009 (Ed.), 2019 Eur. Sp. Power Conf.France.

[4] J. Su, H. Song, C. Wang, J. Su, H. Song, C. Wang, Morphology reshaping enabling self-densification of manganese oxide hybrid materials for high-density lithium storage anodes, (2019). 10.1002/adfm.201907154.

[5] H. Song, J. Su, C. Wang, H. Song, J. Su, C. Wang, CommuniCation 1900426 (1 of 8) *in situ* subangstrom-thick organic engineering enables mono-scale, ultrasmall ZnO nanocrystals for a high initial coulombic efficiency, fully reversible conversion, and cycle-stable Li-ion storage, (2019). 10.1002/aenm.201900426.

[6] S. Goriparti, E. Miele, F. De Angelis, E. Di Fabrizio, R. Proietti Zaccaria, C. Capiglia, Review on recent progress of nanostructured anode materials for Li-ion batteries, J. Power Sources 257 (2014) 421–443, https://doi.org/10.1016/j.jpowsour.2013.11.103.

[7] N. Nitta, F. Wu, J.T. Lee, G. Yushin, Li-ion battery materials: present and future, Mater. Today 18 (2015) 252–264, https://doi.org/10.1016/j.mattod.2014.10.040.

[8] B.O. Varga, A. Sagoian, F. Mariasiu, Prediction of electric vehicle range: a comprehensive review of current issues and challenges, Energies (2019), https://doi.org/10.3390/en12050946.

[9] R.A. Marsh, S. Vukson, S. Surampudi, B.V. Ratnakumar, M.C. Smart, M. Manzo, P. J. Dalton, Li ion batteries for aerospace applications, J. Power Sources (2001), https://doi.org/10.1016/S0378-7753(01)00584-5.

[10] M.C. Smart, B.V. Ratnakumar, L.D. Whitcanack, K.B. Chin, S. Surampudi, R. Gitzendanner, F. Puglia, J. Byers, Lithium-ion batteries for aerospace, IEEE Aerosp. Electron. Syst. Mag. 19 (2004) 18–25, https://doi.org/10.1109/MAES.2004.1263988.

[11] M.N. Obrovac, V.L. Chevrier, Alloy negative electrodes for Li-ion batteries, Chem. Rev. 114 (2014) 11444–11502, https://doi.org/10.1021/cr500207g.

[12] N. Nitta, G. Yushin, High-capacity anode materials for lithium-ion batteries: choice of elements and structures for active particles, Part. Part. Syst. Charact. (2014), https://doi.org/10.1002/ppsc.201300231.

[13] J. Deng, H. Ji, C. Yan, J. Zhang, W. Si, S. Baunack, S. Oswald, Y. Mei, O.G. Schmidt, Naturally rolled-up C/Si/C trilayer nanomembranes as stable anodes for lithium-ion batteries with remarkable cycling performance, Angew. Chem. Int. Ed. 52 (2013) 2326–2330, https://doi.org/10.1002/anie.201208357.

[14] D. Cho, M. Kim, J. Hwang, J.H. Park, Y.L. Joo, Y. Jeong, Facile synthesis of porous silicon nanofibers by magnesium reduction for application in lithium ion batteries, Nanoscale Res. Lett. 10 (2015) 0–7, https://doi.org/10.1186/s11671-015-1132-8.

[15] J. Qin, M. Cao, Multidimensional germanium-based materials as anodes for lithium-ion batteries, Chem. Asian J. 11 (2016) 1169–1182, https://doi.org/10.1002/asia.201600005.

[16] S. Wu, C. Han, J. Iocozzia, M. Lu, R. Ge, R. Xu, Z. Lin, Germanium-based nanomaterials for rechargeable batteries, Angew. Chem Int. Ed. 55 (2016) 7898–7922, https://doi.org/10.1002/anie.201509651.

[17] J. Wang, J.Z. Wang, Z.Q. Sun, X.W. Gao, C. Zhong, S.L. Chou, H.K. Liu, A germanium/single-walled carbon nanotube composite paper as a free-standing anode for lithium-ion batteries, J. Mater. Chem. A 2 (2014) 4613–4618, https://doi.org/10.1039/c3ta14934j.

[18] S. Yoon, C.M. Park, H.J. Sohn, Electrochemical characterizations of germanium and carbon-coated germanium composite anode for lithium-ion batteries, Electrochem. Solid-State Lett. 11 (2008) A42, https://doi.org/10.1149/1.2836481.

[19] L. Liu, F. Xie, J. Lyu, T. Zhao, T. Li, B.G. Choi, Tin-based anode materials with well-designed architectures for next-generation lithium-ion batteries, J. Power Sources 321 (2016) 11–35, https://doi.org/10.1016/j.jpowsour.2016.04.105.

[20] Y. Zhao, X. Li, B. Yan, D. Li, S. Lawes, X. Sun, Significant impact of 2D graphene nanosheets on large volume change tin-based anodes in lithium-ion batteries: a review, J. Power Sources 274 (2015) 869–884, https://doi.org/10.1016/j.jpowsour.2014.10.008.

[21] Y. Zhang, N. Du, C. Xiao, S. Wu, Y. Chen, Y. Lin, J. Jiang, Y. He, D. Yang, Simple synthesis of SiGe@C porous microparticles as high-rate anode materials for lithium-ion batteries, RSC Adv. 7 (2017) 33837–33842, https://doi.org/10.1039/c7ra04364c.

[22] S. Goriparti, U. Gulzar, E. Miele, F. Palazon, A. Scarpellini, S. Marras, S. Monaco, R. Proietti Zaccaria, C. Capiglia, Facile synthesis of Ge–MWCNT nanocomposite electrodes for high capacity lithium ion batteries, J. Mater. Chem. A 5 (2017) 19721–19728, https://doi.org/10.1039/C7TA04971D.

[23] Z. Hu, S. Zhang, C. Zhang, G. Cui, High performance germanium-based anode materials, Coord. Chem. Rev. 326 (2016) 34–85, https://doi.org/10.1016/j.ccr.2016.08.002.

[24] X.H. Liu, S. Huang, S.T. Picraux, J. Li, T. Zhu, J.Y. Huang, Reversible nanopore formation in Ge nanowires during lithiation- delithiation cycling: an *in situ* transmission electron microscopy study, Nano Lett. 11 (2011) 3991–3997, https://doi.org/10.1021/nl2024118.

[25] W. Liang, H. Yang, F. Fan, Y. Liu, X.H. Liu, J.Y. Huang, T. Zhu, S. Zhang, Tough germanium nanoparticles under electrochemical cycling, ACS Nano 7 (2013) 3427–3433, https://doi.org/10.1021/nn400330h.

[26] Y. Liu, X.H. Liu, B.M. Nguyen, J. Yoo, J.P. Sullivan, S.T. Picraux, J.Y. Huang, S. A. Dayeh, Tailoring lithiation behavior by interface and bandgap engineering at the nanoscale, Nano Lett. (2013), https://doi.org/10.1021/nl4027549.

[27] F.S. Ke, K. Mishra, L. Jamison, X.X. Peng, S.G. Ma, L. Huang, S.G. Sun, X.D. Zhou, Tailoring nanostructures in micrometer size germanium particles to improve their performance as an anode for lithium ion batteries, Chem. Commun. 50 (2014) 3713–3715, https://doi.org/10.1039/c4cc00051j.

[28] U. Gulzar, T. Li, X. Bai, S. Goriparti, R. Brescia, C. Capiglia, R.P. Zaccaria, Nitrogen-doped single walled carbon nanohorns enabling effective utilization of Ge nanocrystals for next generation lithium ion batteries, Electrochim. Acta 298 (2019) 89–96, https://doi.org/10.1016/j.electacta.2018.11.130.

[29] Y. Sun, S. Jin, G. Yang, J. Wang, C. Wang, Germanium nanowires-in-graphite tubes via self-catalyzed synergetic confined growth and shell-splitting enhanced Li-storage performance, ACS Nano 9 (2015) 3479–3490, https://doi.org/10.1021/nn506955f.

[30] B. Farbod, K. Cui, M. Kupsta, W.P. Kalisvaart, E. Memarzadeh, A. Kohandehghan, B. Zahiri, D. Mitlin, Array geometry dictates electrochemical performance of Ge nanowire lithium ion battery anodes, J. Mater. Chem. A 2 (2014) 16770–16785, https://doi.org/10.1039/c4ta03805c.

[31] M.H. Park, Y. Cho, K. Kim, J. Kim, M. Liu, J. Cho, Germanium nanotubes prepared by using the Kirkendall effect as anodes for high-rate lithium batteries, Angew. Chem. Int. Ed. 50 (2011) 9647–9650, https://doi.org/10.1002/anie.201103062.

[32] C. Zhang, Z. Lin, Z. Yang, D. Xiao, P. Hu, H. Xu, Y. Duan, S. Pang, L. Gu, G. Cui, Hierarchically designed germanium microcubes with high initial Coulombic efficiency toward highly reversible lithium storage, Chem. Mater. 27 (2015) 2189–2194, https://doi.org/10.1021/acs.chemmater.5b00218.

[33] U. Gulzar, T. Li, X. Bai, M. Colombo, A. Ansaldo, S. Marras, M. Prato, S. Goriparti, C. Capiglia, R.P Zaccaria, Nitrogen-doped single-walled carbon nanohorns as a cost-effective carbon host toward high-performance lithium−sulfur batteries, ACS Appl. Mater. Interfaces 10 (2018) 56, https://doi.org/10.1021/acsami.7b17602.

[34] A. Casimir, H. Zhang, O. Ogoke, J.C. Amine, J. Lu, G. Wu, Silicon-based anodes for lithium-ion batteries: effectiveness of materials synthesis and electrode preparation, Nano Energy (2016), https://doi.org/10.1016/j.nanoen.2016.07.023.

[35] D.L. Wood, J. Li, C. Daniel, Prospects for reducing the processing cost of lithium ion batteries, J. Power Sources (2015), https://doi.org/10.1016/j.jpowsour.2014.11.019.

[36] Y.D. Ko, J.G. Kang, G.H. Lee, J.G. Park, K.S. Park, Y.H. Jin, D.W. Kim, Sn-induced low-temperature growth of Ge nanowire electrodes with a large lithium storage capacity, Nanoscale 3 (2011) 3371–3375, https://doi.org/10.1039/c1nr10471c.

[37] C.K. Chan, X.F. Zhang, Y. Cui, High capacity Li ion battery anodes using Ge nanowires, Nano Lett. 8 (2008) 307–309, https://doi.org/10.1021/nl0727157.

[38] T. Kennedy, E. Mullane, H. Geaney, M. Osiak, C. O'Dwyer, K.M. Ryan, High-performance germanium nanowire-based lithium-ion battery anodes extending over 1000 cycles through *in situ* formation of a continuous porous network, Nano Lett. 14 (2014) 716–723, https://doi.org/10.1021/nl403979s.

[39] E. Mullane, T. Kennedy, H. Geaney, K.M. Ryan, A rapid, solvent-free protocol for the synthesis of germanium nanowire lithium-ion anodes with a long cycle life and high rate capability, ACS Appl. Mater. Interfaces 6 (2014) 18800–18807, https://doi.org/10.1021/am5045168.

[40] C. Rosenblad, H.R. Deller, A. Dommann, T. Meyer, P. Schroeter, H. von Känel, Silicon epitaxy by low-energy plasma enhanced chemical vapor deposition, J. Vac. Sci. Technol. A 16 (1998) 2785–2790, https://doi.org/10.1116/1.581422. Vacuum, Surfaces, Film.

[41] M. Kummer, C. Rosenblad, A. Dommann, T. Hackbarth, G. Höck, M. Zeuner, E. Müller, H. Von Känel, Low energy plasma enhanced chemical vapor deposition, Mater. Sci. Eng. B 89 (2002) 288–295, https://doi.org/10.1016/S0921-5107(01)00801-7. Solid-State Mater. Adv. Technol.

[42] K. Stokes, W. Boonen, H. Geaney, T. Kennedy, D. Borsa, K.M. Ryan, Tunable core-shell nanowire active material for high capacity Li-ion battery anodes comprised of PECVD deposited aSi on directly grown Ge nanowires, ACS Appl. Mater. Interfaces (2019), https://doi.org/10.1021/acsami.9b03931.

[43] E. Garralaga Rojas, B. Terheiden, H. Plagwitz, J. Hensen, C. Baur, G.F.X. Strobl, R. Brendel, Formation of mesoporous germanium double layers by electrochemical etching for layer transfer processes, Electrochem. Commun. (2010), https://doi.org/10.1016/j.elecom.2009.11.033.

[44] E. Garralaga Rojas, J. Hensen, J. Carstensen, H. Föll, R. Brendel, Porous germanium multilayers, Phys. Status Solidi (2011), https://doi.org/10.1002/pssc.201000130. Curr. Top. Solid State Phys.

[45] G. Calabrese, S. Baricordi, P. Bernardoni, S. Fin, V. Guidi, D. Vincenzi, Towards III-V solar cells on Si: improvement in the crystalline quality of Ge-on-Si virtual substrates through low porosity porous silicon buffer layer and annealing, AIP Conf. Proc. 1616 (2014) 37–40, https://doi.org/10.1063/1.4897023.

[46] D.R. Turner, On the mechanism of chemically etching germanium and silicon, J. Electrochem. Soc. 107 (1960) 810–816, https://doi.org/10.1149/1.2427519.

[47] S. Tutashkonko, A. Boucherif, T. Nychyporuk, A. Kaminski-Cachopo, R. Arès, M. Lemiti, V. Aimez, Mesoporous germanium formed by bipolar electrochemical etching, Electrochim. Acta 88 (2013) 256–262, https://doi.org/10.1016/j.electacta.2012.10.031.

[48] Y.A. Bioud, A. Boucherif, A. Belarouci, E. Paradis, S. Fafard, V. Aimez, D. Drouin, R. Arès, Fast growth synthesis of mesoporous germanium films by high frequency bipolar electrochemical etching, Electrochim. Acta (2017), https://doi.org/10.1016/j.electacta.2017.02.115.
[49] Y. Jin, N.J.H. Kneusels, L.E. Marbella, E. Castillo-Martínez, P.C.M.M. Magusin, R. S. Weatherup, E. Jónsson, T. Liu, S. Paul, C.P. Grey, Understanding fluoroethylene carbonate and vinylene carbonate based electrolytes for Si anodes in lithium ion batteries with NMR spectroscopy, J. Am. Chem. Soc. 140 (2018) 9854–9867, https://doi.org/10.1021/jacs.8b03408.
[50] A.M. Chockla, K.C. Klavetter, C.B. Mullins, B.A. Korgel, Solution-grown germanium nanowire anodes for lithium-ion batteries, ACS Appl. Mater. Interfaces 4 (2012) 4658–4664, https://doi.org/10.1021/am3010253.
[51] A.L. Michan, B.S. Parimalam, M. Leskes, R.N. Kerber, T. Yoon, C.P. Grey, B. L. Lucht, Fluoroethylene carbonate and vinylene carbonate reduction: understanding lithium-ion battery electrolyte additives and solid electrolyte interphase formation, Chem. Mater. 28 (2016) 8149–8159, https://doi.org/10.1021/acs.chemmater.6b02282.
[52] S.S. Zhang, A review on electrolyte additives for lithium-ion batteries, J. Power Sources 162 (2006) 1379–1394, https://doi.org/10.1016/j.jpowsour.2006.07.074.
[53] C. Chae, H. Noh, J.K. Lee, B. Scrosati, Y. Sun, FULL PAPER a high-energy Li-ion battery using a silicon-based anode and a nano-structured layered composite cathode, (2014) 3036–3042. 10.1002/adfm.201303766.
[54] Y. Gao, A new secondary ion mass spectrometry technique for III-V semiconductor compounds using the molecular ions CsM+, J. Appl. Phys. (1988) https://doi.org/10.1063/1.341381.
[55] M. Bersani, D. Giubertoni, E. Iacob, M. Barozzi, S. Pederzoli, L. Vanzetti, M. Anderle, Boron ultralow energy SIMS depth profiling improved by rotating stage, Appl. Surf. Sci. 252 (2006) 7315–7317, https://doi.org/10.1016/j.apsusc.2006.02.282.
[56] S.J. An, J. Li, C. Daniel, D. Mohanty, S. Nagpure, D.L. Wood, The state of understanding of the lithium-ion-battery graphite solid electrolyte interphase (SEI) and its relationship to formation cycling, Carbon N. Y. 105 (2016) 52–76, https://doi.org/10.1016/j.carbon.2016.04.008.
[57] S.J. An, J. Li, Z. Du, C. Daniel, D.L. Wood, Fast formation cycling for lithium ion batteries, J. Power Sources (2017), https://doi.org/10.1016/j.jpowsour.2017.01.011.
[58] B.A. Boukamp, A nonlinear least squares fit procedure for analysis of immittance data of electrochemical systems, Solid State Ion. 20 (1986) 31–44, https://doi.org/10.1016/0167-2738(86)90031-7.
[59] J. Ross Macdonald, Note on the parameterization of the constant-phase admittance element, Solid State Ion. (1984), https://doi.org/10.1016/0167-2738(84)90049-3.
[60] B.A. Boukamp, A package for impedance/admittance data analysis, Solid State Ion. 18–19 (1986) 136–140, https://doi.org/10.1016/0167-2738(86)90100-1.
[61] NIST X-ray photoelectron spectroscopy database, version 4.1 National Institute of Standards and Technology, Gaithersburg, (2012). http://srdata.nist.gov/xps/.
[62] G. Zhao, N. Zhang, K. Sun, Electrochemical preparation of porous MoO_3 film with a high rate performance as anode for lithium ion batteries, J. Mater. Chem. A (2013), https://doi.org/10.1039/c2ta00361a.
[63] Y. Shi, B. Guo, S.A. Corr, Q. Shi, Y.S. Hu, K.R. Heier, L. Chen, R. Seshadri, G. D. Stucky, Ordered mesoporous metallic MoO_2 materials with highly reversible lithium storage capacity, Nano Lett. 9 (2009) 4215–4220, https://doi.org/10.1021/nl902423a.
[64] Y. Xu, R. Yi, B. Yuan, X. Wu, M. Dunwell, Q. Lin, L. Fei, S. Deng, P. Andersen, D. Wang, H. Luo, High capacity MoO_2/graphite oxide composite anode for lithium-ion batteries, J. Phys. Chem. Lett. 3 (2012) 309–314, https://doi.org/10.1021/jz201619r.
[65] U.K. Sen, S. Mitra, Synthesis of molybdenum oxides and their electrochemical properties against li, Energy Procedia (2014) 740–747, https://doi.org/10.1016/j.egypro.2014.07.315.
[66] Y. Sun, X. Hu, W. Luo, Y. Huang, Self-assembled hierarchical MoO_2/graphene nanoarchitectures and their application as a high-performance anode material for lithium-ion batteries, ACS Nano 5 (2011) 7100–7107, https://doi.org/10.1021/nn201802c.
[67] C. Zhong, J.Z. Wang, X.W. Gao, D. Wexler, H.K. Liu, *In situ* one-step synthesis of a 3D nanostructured germanium-graphene composite and its application in lithium-ion batteries, J. Mater. Chem. A 1 (2013) 10798–10804, https://doi.org/10.1039/c3ta11796k.
[68] J.B. Goodenough, Y. Kim, Challenges for rechargeable Li batteries, Chem. Mater. (2010), https://doi.org/10.1021/cm901452z.
[69] B.V. Ratnakumar, M.C. Smart, A. Kindler, H. Frank, R. Ewell, S. Surampudi, Lithium batteries for aerospace applications: 2003 mars exploration rover, J. Power Sources (2003), https://doi.org/10.1016/S0378-7753(03)00220-9.
[70] K.L. Chopra, S.K. Bahl, Structural, electrical, and optical properties of amorphous germanium films, Phys. Rev. B (1970), https://doi.org/10.1103/PhysRevB.1.2545.
[71] A.K. Padhi, K.S. Nanjundaswamy, J.B. Goodenough, Phospho-olivines as positive-electrode materials for rechargeable lithium batteries, J. Electrochem. Soc. (1997), https://doi.org/10.1149/1.1837571.
[72] J. Li, C. Arbizzani, S. Kjelstrup, J. Xiao, Y. Yao Xia, Y. Yu, Y. Yang, I. Belharouak, T. Zawodzinski, S.T. Myung, R. Raccichini, S. Passerini, Good practice guide for papers on batteries for the journal of power sources, J. Power Sources (2020), https://doi.org/10.1016/j.jpowsour.2020.227824.
[73] J. Graetz, C.C. Ahn, R. Yazami, B. Fultz, Nanocrystalline and thin film germanium electrodes with high lithium capacity and high rate capabilities, J. Electrochem. Soc. 151 (2004) 698–702, https://doi.org/10.1149/1.1697412.
[74] K. Mishra, X.C. Liu, F.S. Ke, X.D. Zhou, Porous germanium enabled high areal capacity anode for lithium-ion batteries, Compos. Part B Eng. (2019), https://doi.org/10.1016/j.compositesb.2018.10.076.
[75] E.A. Saverina, V. Sivasankaran, R.R. Kapaev, A.S. Galushko, V.P. Ananikov, M. P. Egorov, V.V. Jouikov, P.A. Troshin, M.A. Syroeshkin, An environment-friendly approach to produce nanostructured germanium anodes for lithium-ion batteries, Green Chem. (2020), https://doi.org/10.1039/c9gc02348h.
[76] X. Li, Z. Yang, Y. Fu, L. Qiao, D. Li, H. Yue, D. He, Germanium anode with excellent lithium storage performance in a germanium/lithium-cobalt oxide lithium-ion battery, ACS Nano 9 (2015) 1858–1867, https://doi.org/10.1021/nn506760p.
[77] S. Liu, J. Feng, X. Bian, Y. Qian, J. Liu, H. Xu, Nanoporous germanium as high-capacity lithium-ion battery anode, Nano Energy 13 (2015) 651–657, https://doi.org/10.1016/j.nanoen.2015.03.039.
[78] L.C. Yang, Q.S. Gao, L. Li, Y. Tang, Y.P. Wu, Mesoporous germanium as anode material of high capacity and good cycling prepared by a mechanochemical reaction, Electrochem. Commun. (2010), https://doi.org/10.1016/j.elecom.2010.01.008.
[79] K.C. Klavetter, S.M. Wood, Y.M. Lin, J.L. Snider, N.C. Davy, A.M. Chockla, D. K. Romanovicz, B.A. Korgel, J.W. Lee, A. Heller, C.B. Mullins, A high-rate germanium-particle slurry cast Li-ion anode with high Coulombic efficiency and long cycle life, J. Power Sources (2013), https://doi.org/10.1016/j.jpowsour.2013.02.091.